

DIA Photometry and Gravitational Microlensing

Third Year Lab Report

Euan Baldwin 10818421

Department of Physics and Astronomy, University of Manchester

(Experiment performed in collaboration with Luca Vicaria 10828724)

(Dated: May 3, 2024)

This report presents an analysis of gravitational microlensing events through the application of difference image photometry, utilising data from the Andromeda Galaxy Stellar Robotic Microlensing (Angstrom) Project. Several potential microlensing events are identified within the dataset. The prime microlensing candidate is an object with mass $0.022 \pm 0.018M_{\odot}$, implying a brown dwarf star. Additionally, a higher mass microlensing event, $9 \pm 8M_{\odot}$, and a double microlensing event are detected, alongside the observation of a nova. This study underscores the utility of microlensing for identifying and characterising astronomical bodies.

1. INTRODUCTION

Gravitational microlensing, a phenomenon predicted by Einstein's theory of general relativity, has become an invaluable tool in astrophysics for detecting objects that emit little or no light. The technique relies on the bending of light from a background star by a foreground object. This magnifies the star's light and can reveal the presence of otherwise invisible matter in the universe. Gravitational microlensing differs from gravitational lensing as it occurs when the mass of the lensing object is relatively small and, instead of creating multiple resolvable images, it can only be detected through changes in electromagnetic flux over time [1].

Although predicted in the early 20th century, it was not until the 1980s and 1990s that advancements in technology permitted the observation of microlensing events [2]. Initially, microlensing was proposed to detect Massive Compact Halo Objects in galactic halos, thought to account for dark matter [3]. However, it's now understood that dark matter is primarily non-baryonic, shifting the focus of microlensing. Today, microlensing is instrumental in exploring the Milky Way's structure and detecting objects in other galaxies like stellar-mass black holes, brown dwarfs, and exoplanets [4].

Microlensing is particularly effective in crowded stellar fields, such as those towards the Galactic Bulge or in nearby galaxies like Andromeda (M31). These areas provide a dense backdrop of stars, essential for the chance alignments (that occur in approximately one in a million stars) required for microlensing. This paper will investigate the detection of new astronomical objects in M31.

2. METHODOLOGY

2.1. Data Collection

The Andromeda Galaxy Stellar Robotic Microlensing (Angstrom) Project has been at the forefront of microlensing detection for the last few decades, employing a distributed network of telescopes to monitor millions of stars in M31 [5]. The Angstrom Project is an international initiative, with astronomers collaborating to probe the M31 bulge through a network of 2m-class Northern Hemisphere optical telescopes. These conduct several observations every day throughout the M31 viewing season, extending from August to February.

The telescopes employ Sloan i and Cousins I filters to effectively distinguish microlensing events from periodic variables, such as Miras, which are most prominent in these bands. The specifics of each telescope and camera are detailed in Table I. The observation protocols consist of thirty-minute exposures, which compile several shorter

exposures to avoid saturation at the core of the bulge. This report examines 481 observations from the Angstrom network, spanning five viewing seasons from 2004/5 to 2008/9. The data then undergoes difference image analysis to identify microlensing events amid the background stellar variability and noise.

Telescope	Field of view (arcmins)	Camera size (pixels)	Filter
2m LT, La Palma	4.6	2k x 2k	Sloan i
2m FTN, Hawaii	4.6	2k x 2k	Sloan i
1.5m Maidanak, Uzbek.	18	4k x 4k	Cousins I
1.8m BOAO, S. Korea	11	2k x 2k	Cousins I
2.4m MDM, Arizona	4.6	1k x 1k	Cousins I

TABLE I. The Angstrom Project's telescopes and camera characteristics. Taken from [5].

2.2. Difference Image Analysis

Difference Image Analysis (DIA) is a computational technique that detects and quantifies variations in astronomical images by subtracting a well-calibrated reference image from target images. The effectiveness of DIA is dependent upon the fidelity of the reference image since any defects are propagated onto all subsequent difference images. The noise present in the difference image is a function of the noise in both the reference and the target images, and enhancing the signal-to-noise ratio of the reference image can be achieved by stacking multiple exposures to create a superior master reference image, reducing noise as the square root of the number of combined images.

An optimal reference image is comprised of images that share the following characteristics: a compact, circular point spread function (PSF) indicated by good seeing and accurate telescope tracking; a minimal level of background light from natural and artificial pollution; high photon count levels per unit exposure time, indicated by a low air-mass; and minimal image defects due to cosmic ray strikes and defective CCD columns. A selection process is undertaken to build a catalogue of ten images with these characteristics, with which to build the reference image. First, rough selection criteria, specifying a low seeing, low air-mass and average background, are applied to eliminate the tails of the distributions. Next, harsher selection criteria are implemented, shown in Figure 1, which cut the number of images down to thirty. These thirty images are then inspected manually for seeing, artefacts and misalignment to select the ten highest quality images with which to build the reference image.

The reference image, R , is then adjusted through convolution and flux alignment to match the target image, T . The derived image, R' , is subtracted from T to produce a

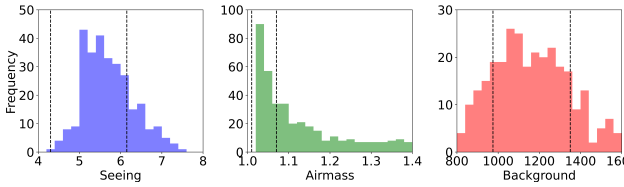


FIG. 1. Image selection cuts for seeing, airmass and background. The dashed lines show the cuts. For an image to progress to manual selection, it must pass all three cuts.

difference image, D , capturing genuine stellar flux variations. Proper alignment of T is essential to ensure accurate superposition of corresponding objects.

Assuming that the precision of DIA is fundamentally limited by photon noise, the difference image between aligned images R_i and T_i is optimised by minimising the sum of squared differences:

$$\sum_i D_i^2 = \min \sum_i (R'_i - T_i + B_i)^2, \quad (1)$$

where R'_i is the result of convolving R_i with kernel K_i , and B_i is the differential background model. The convolution kernel, K_i , consists of three bivariate Gaussians, each warped by a low-order two-dimensional polynomial [6].

In the initial stage of parameter optimisation for K and B , a broad-spectrum heuristic is employed to approximate the global minimum on a set of ten representative images, distinguishing it from potential local minima. This is subsequently refined by adopting a methodical strategy, wherein all variables save one are held constant, allowing for the optimisation of the remaining variable within the phase space.

Integrated Spectrographic Innovative Software [7] then processes the difference images to generate light curves by aggregating absolute pixel values from the difference images to map variable source positions. It then determines the centroid positions of sources above a defined flux threshold and employs PSF-fitting photometry to measure source flux, constructing a variability map, as shown in Figure 2, from which light curves are derived. Outliers, more than 5σ from subsequent fits, are scrutinised and excluded only if significant image defects are identified.

2.3. Modelling Light Curves

To effectively model the light curves derived from DIA, it is crucial to gain an understanding of microlensing events. If a compact object of mass M , at distance D_L from the observer, lies exactly on the line of sight to a background source at distance D_S , the light deflection by general relativity causes the source to appear as an Einstein ring. The time taken to cross the angular radius of this ring, relative to the source, θ_E , is known as the Einstein radius crossing time, t_E .

The core model employed in most microlensing analyses is the point-source point-lens (PSPL) approximation, which adequately describes ninety per cent of microlensing events in the Milky Way. This model presumes a singular lens and source, both of which are sufficiently small compared to the Einstein radius, θ_E , to render their angular sizes negligible [8].

In contrast, microlensing events in M31 face substantial theoretical challenges. The higher background brightness in M31 means that microlensing events typically require significant magnification to be detectable. This is referred to as the pixel-lensing regime, where blending is more pronounced, and the conventional methods for extracting in-

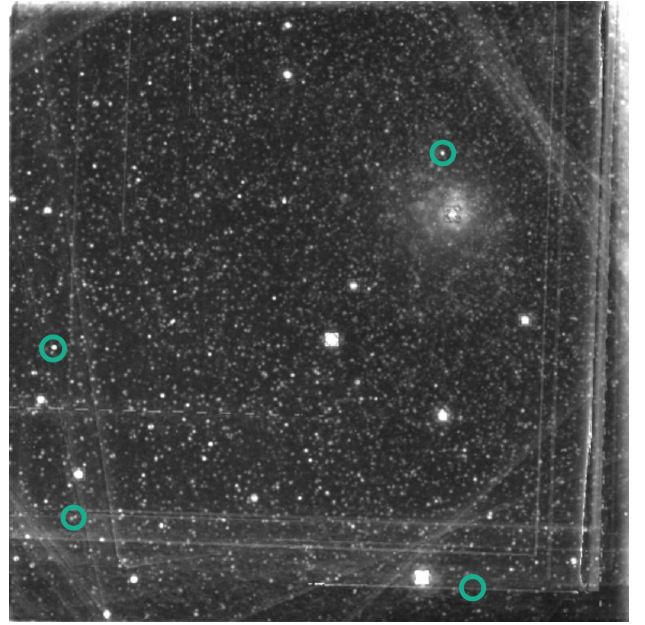


FIG. 2. Variability map showing a region of M31. The core of the M31 bulge is located in the top right. The variable objects of interest are circled in green. Moving clockwise from the bottom-left the light curves are lc876, lc609, lc4927 and lc5293.

dividual light curve parameters, such as t_E , are often infeasible. Instead, the light curve is characterised by:

$$F(t) = F_{\text{base}} + \frac{\Delta F_0}{\sqrt{1 + 12 \left(\frac{t - t_0}{t_{1/2}} \right)^2}}, \quad (2)$$

where F_{base} is the baseline flux, ΔF_0 the flux deviation at peak magnification, and $t_{1/2}$ the event duration measured at half maximum intensity.

In this regime, where ΔF and $t_{1/2}$ are degenerate, the peak magnification constraint that $A_0 > 10$ allows for the approximation:

$$t_E \approx \frac{t_{1/2}}{2\sqrt{3}} A_0. \quad (3)$$

The lower limit on the mass, M , of the lensing object is then calculated from:

$$M = \frac{c^2 \mu_{\text{rel}}^2 t_E^2}{4G} \frac{D_S - D_L}{D_S D_L}, \quad (4)$$

where c represents the speed of light in a vacuum, μ_{rel} is the relative proper motion between the lens and source, and G is the gravitational constant. The statistical uncertainty in the mass, σ_M , is derived through standard error propagation techniques.

3. RESULTS

An example of a light curve, lc876, is shown in Figure 3. Here F_{base} has been modelled as a sinusoidal function. For the other light curves investigated from Figure 2 - lc609, lc4927 and lc5293 - F_{base} was not found to be periodic and hence this step was not required. One of the light curves, lc609, was modelled as a bifurcated microlensing event, lc609-I and lc609-II.

To calculate the masses of the objects of interest we assume D_S to be 780 kpc, D_L to be 782 ± 1 kpc [9] and μ_{rel} to be 3.5 ± 1.3 microarcseconds per year [10]. These assumptions result in the masses shown in Table II. The high

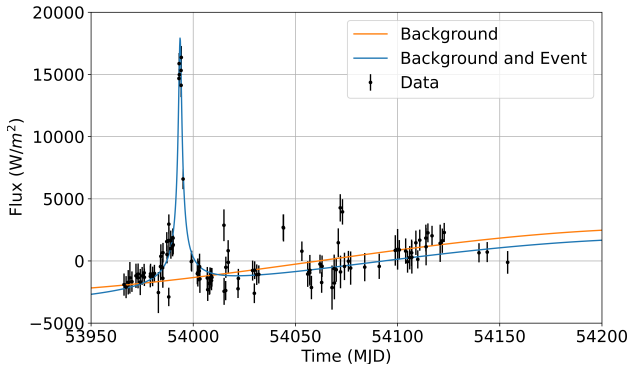


FIG. 3. Recorded flux over time in days (modified Julian Date) for lc876's region of interest. The background is modelled as a sinusoidal function and the microlensing candidate is modelled by Equation 2. The χ^2_R of the model is 1.13.

light curve	t_E (days)	σ_{t_E} (days)	M (M_\odot)	σ_M (M_\odot)	χ^2_R
609-I	34	2	0.4	0.3	0.86
609-II	20.1	1.8	0.14	0.11	0.86
876	8.0	0.8	0.022	0.018	1.13
4927	217	30	16	13	3.38
5293	157	47	9	8	0.93

TABLE II. The lower limit on the Einstein crossing time (days) and the mass of the microlensing object (solar masses) and their respective uncertainties for each light curve. The χ^2_R of each microlensing model is also given.

relative uncertainties in D_L and μ_{rel} translate to a relative uncertainty in the mass of order unity.

As shown in Table II, the χ^2_R of lc876 suggests that it was indeed a microlensing event with a lower bound mass of $0.022 \pm 0.018 M_\odot$. Similarly, lc5293 was a higher mass microlensing event with $M = 9 \pm 8 M_\odot$. The χ^2_R of lc4927 was outside of the acceptable bounds ($0.5 < \chi^2_R < 2.0$) and the shape of the light curve was more indicative of a different type of variable source, rather than microlensing. Lc609 was more complex and required a bifurcated microlensing model, resulting in a χ^2_R towards the lower end of the acceptable range.

4. DISCUSSION

The mass of lc876 implies it is likely to be a brown dwarf, as the mass is consistent with their accepted mass of $0.0125 - 0.0750 M_\odot$ [11]. Additionally, the observed periodicity in the baseline flux could indicate the presence of a variable star, likely a Cepheid due to the symmetry of the periodicity, in the background.

For lc5293, the extended t_E and high mass suggest classification as a stellar-mass black hole. The assessment of its mass, however, must consider the microlensing parallax

effect, notable in long-duration events due to Earth's orbital movement. This effect, while sometimes significant, adds marginal uncertainty here due to the pre-existing substantial uncertainties in μ_{rel} [12]. Moreover, the increase in flux caused by the event was still ongoing when the observing season ended, compounding the difficulties in interpreting the light curve.

Lc4927 is unlikely to be a microlensing event, with its asymmetric light curve instead closely resembling that of a nova. A nova's light curve is characterised by an initial sharp increase in flux, followed by a dust cloud which briefly obscures the event [13].

The light curve of lc609 was best described by a model incorporating two separate microlensing events, resulting in mass estimates consistent with brown dwarf classification. While the fit is ostensibly robust ($\chi^2_R = 0.86$), the approach led to a near-complete degeneracy in the model parameters. Moreover, the probability of two independent microlensing events affecting a source star is highly remote, with the incidence of any star undergoing microlensing estimated at approximately one in a million [14]. To achieve more accurate mass determinations in such systems, the adoption of advanced modelling approaches is essential. Specifically, the application of binary lens equations, as discussed in recent studies [15], is recommended to address these complexities.

Other potential improvements to the analysis include the use of machine learning algorithms to search the convolution kernel and background noise parameter optimisation phase space. This would enable a more thorough search for the optimal parameters, potentially improving the quality of the data at later stages in the DIA pipeline. Furthermore, the automation of the process of identifying and fitting light curves to candidate events would allow for a larger catalogue of events to be studied.

5. CONCLUSIONS

We have identified various astronomical objects, including a brown dwarf of mass $0.022 \pm 0.018 M_\odot$, a black hole of mass $9 \pm 8 M_\odot$, and a binary microlensing event. The asymmetric light curve of a nova was also observed. Several improvements to the experimental techniques are suggested, including the use of a binary lens model to interpret double microlensing light curves. Additionally, the integration of machine learning algorithms could significantly improve the optimisation procedure for model parameters, thereby improving the accuracy of the latter stages of the DIA pipeline. Overall, this investigation has reaffirmed the use of gravitational microlensing as a powerful astronomical tool, providing crucial insights into the composition of the Andromeda Galaxy.

[1] S. Mao, in *Manchester Microlensing Conference* (2008).
[2] K. Chang and S. Refsdal, *Nature* **282**, 561 (1979).
[3] B. Paczynski, *Astrophysical Journal* **304**, 1 (1986).
[4] I. A. Bond *et al.*, *Astrophysical Journal* **606**, 155 (2004).
[5] E. Kerins, in *Manchester Microlensing Conference* (2008).
[6] C. Alard and R. H. Lupton, *Astrophysical Journal* **503**, 325 (1998).
[7] J. C. Houck *et al.*, in *Astronomical Data Analysis Software and Systems IX*, Astronomical Society of the Pacific Conference Series, Vol. 216 (2000) p. 591.
[8] W. Sutherland, *Rev. Mod. Phys.* **71**, 421 (1999).
[9] A. G. Riess *et al.*, *Astrophysical Journal* **745**, 156 (2012).

[10] E. Kerins, DIA photometry and gravitational microlensing (2021), Laboratory Script.
[11] B. Zuckerman, *Proceedings of the National Academy of Sciences* **97**, 963 (2000).
[12] D. Bennett *et al.*, *Astrophysical Journal* **579**, 639 (2002).
[13] I. Hachisu and M. Kato, *Astrophysical Journal Supplement Series* **242**, 18 (2019).
[14] S. Mao and B. Paczynski, *Astrophysical Journal* **374**, 37 (1991).
[15] R. Poleski and J. C. Yee, *Astronomy and Computing* **26**, 35 (2019).